Bio-Design and Manufacturing
https://doi.org/10.1631/bdm.2400114

RESEARCH ARTICLE

Enhancing angiogenesis and osseointegration through a double gyroid Ti6Al4V scaffold with triply periodic minimal surface

Hao Liu[1] · Hao Chen[1] · Bin Sun[1] · Danyang Fan[2] · Aobo Zhang[1] · Hanqiang Liu[1] · Hexiang Wei[1] · Wenbo Yang[1] · Yongyue Li[1] · Peng Xia[1] · Qing Han[1] · Jincheng Wang[1]

Received: 27 March 2024 / Accepted: 15 September 2024

Abstract

The pore structure of porous scaffolds plays a crucial role in bone repair. The prevalent bone implant structure in clinical practice is the traditional cubic structure. However, the traditional cubic structure exhibits sharp edges and junctions that are not conducive to cell adhesion and growth. In this study, a double gyroid (DG) Ti6Al4V scaffold based on a triply periodic minimal surface (TPMS) structure was devised, and the osseointegration performance of DG structural scaffolds with varying porosities was investigated. Compression tests revealed that the elastic modulus and compressive strength of DG structural scaffolds were sufficient for orthopedic implants. In vitro cellular experiments demonstrated that the DG structure significantly enhanced cell proliferation, vascularization, and osteogenic differentiation compared to the cubic structure. The DG structure with 55% porosity exhibited the most favorable outcomes. In vivo experiments in rabbits further demonstrated that DG scaffolds could promote neovascularization and bone regeneration and maturation; those with 55% porosity performed best. Comparing the surface area, specific surface area per unit volume, and internal flow distribution characteristics of gyroid and DG structure scaffolds, the latter are more conducive to cell adhesion and growth within scaffolds. This study underscored the potential of DG scaffolds based on the TPMS structure in optimizing the pore structure design of titanium scaffolds, inducing angiogenesis, and advancing the clinical application of titanium scaffolds for repairing bone defects.

Hao Liu and Hao Chen have contributed equally to this work.

✉ Peng Xia
xiapeng@jlu.edu.cn

✉ Qing Han
my.hanqing@163.com

[1] Department of Orthopedic Surgery, The Second Hospital of Jilin University, Changchun 130000, Jilin, China

[2] Department of Dermatology, The Second Hospital of Jilin University, Changchun 130000, Jilin, China

Graphic abstract

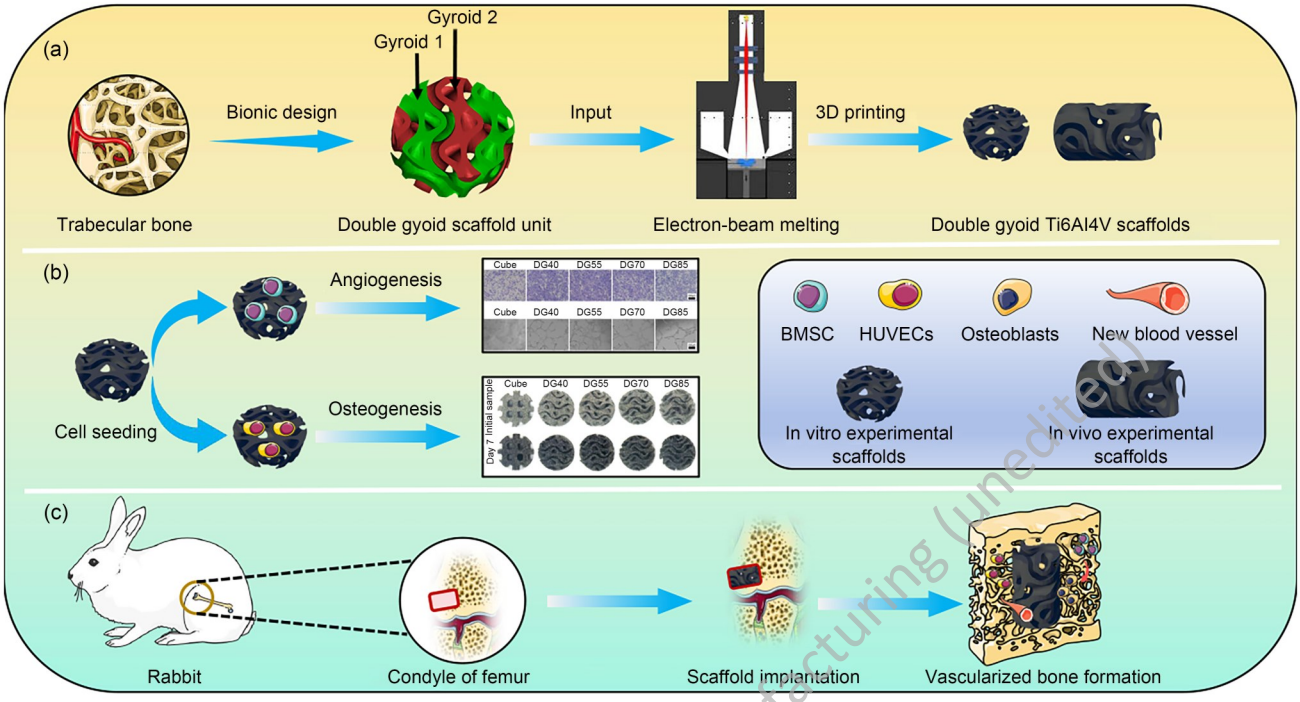

Keywords Double gyroid · Triply periodic minimal surface · Osseointegration · Angiogenesis

1 Introduction

Repair of critical-size bone defects caused by trauma, tumors, inflammation, and other bone diseases remains an urgent clinical problem in orthopedics [1]. Autografts or allografts are commonly used to repair such bone defects in clinical practice [2]. However, autologous bone is limited in access and prone to combined donor area damage, and allogeneic bone carries the risk of immune rejection and disease transmission [3, 4]. Bone tissue engineering (BTE) is one of the most promising strategies to replace the above treatment options, in which titanium alloys have been used in clinical practice for >40 years due to their excellent mechanical properties, biocompatibility, and corrosion resistance [5]. However, the elastic modulus of solid titanium alloys is higher than that of natural bone, and their direct use as implants has a stress shielding effect [6, 7]. The stress shielding effect reduces the mechanical load on the bone surrounding the implant, leading to bone resorption and loosening of the implant [8]. The introduction of a porous design allows the elastic modulus of the implant to be reduced, avoiding the stress shielding effect [9]. Importantly, the porous structure provides effective space for inward bone growth and promotes rapid bone formation and integration at the bone implant interface [10]. Kuboki et al. [11] compared the osteogenic properties of hydroxyapatite in solid and porous structures using a mouse subcutaneous model and found that osteogenesis occurred only in porous structures. The properties of the porous structure (e.g., pore shape and porosity) affect the growth condition of cells inside scaffolds [12]. Wu et al. [13] compared the early vascularization behavior of scaffolds with strut-based and curved pore structures and found that scaffolds with curved pore structures were more conducive to early angiogenesis. Scaffold porosity is also important for cell growth [14]. Higher porosity is more beneficial for inward bone growth, but scaffold strength is reduced [15]. Therefore, multiple factors should be considered when designing porous scaffolds to promote angiogenesis and bone formation while ensuring scaffold strength [16].

Among many porous structures, triply periodic minimal surface (TPMS) structures have received much attention due to their similarity to cancellous bone structures. The mean curvature of bone trabeculae is close to 0, and that of TPMS structures is also 0, giving TPMS structures a natural bionic advantage [17]. TPMS structures offer many advantages over classical lattice and foam structures. First, their basic properties (e.g., porosity and bulk-specific surface area) can be precisely controlled by adjusting mathematical functions.

Second, the smooth and continuous surface of TPMS is more beneficial for cell adhesion and multiplication [18]. These special structural properties make TPMS particularly suitable for manufacturing bone scaffolds or surface structures for implants [19]. Yang et al. [20] found that compared to traditional lattice scaffolds, TPMS scaffolds with a wave shape could induce cytoskeletal reorganization and nuclear deformation, directing osteogenic differentiation and angiogenic paracrine secretion of mesenchymal stem cells (MSCs) and accelerating bone regeneration. The most common TPMS structures used in BTE include gyroid, primitive, and diamond [21]. The gyroid structure has higher permeability and is more favorable for cell seeding, infiltration, and differentiation [22]. Two structures can be efficiently created using TPMS: skeleton and sheet structures [23]. The sheet structure shows better mechanical properties than the skeleton structure [24]; thus, the sheet structure of TPMS is chosen to construct the bone scaffold in this study.

TPMS-based porous structures have several advantages in terms of mechanical properties, osteogenic capacity, and vascularity, and further optimization of TPMS scaffolds for BTE has a promising future [18]. The porous bone scaffold lightweight structure design aims to find a balance between material consumption and overall performance, which means that the appropriate pores need to be designed in ideal locations for optimum performance [25]. Most research in BTE involving TPMS structures focuses on comparing different TPMS structures or contrasting TPMS structures with strut-node lattice structures. For example, Maevskaia et al. [26] compared the performance of three classic TPMS structures (diamond, gyroid, and primitive) with traditional lattice structures as orthopedic implants. Li et al. [27] explored the effects of TPMS structures, cylindrical scaffolds, and cubic scaffolds on osteogenesis and angiogenesis in vitro and in vivo. However, there is limited research on the optimal porosity of a specific TPMS structure. Therefore, this study combined two sheet-like gyroid structures based on TPMS to design and fabricate four double gyroid (DG) titanium alloy scaffolds with different porosities (40%, 55%, 70%, and 85%). Based on previous studies, this study fabricated a classic cubic structure titanium alloy scaffold with 70% porosity as a control group [28, 29]. The differences between the DG and cubic structure in terms of osteogenesis and angiogenesis were compared, and the optimal porosity of the DG structure for bone growth and blood vessel formation was investigated. Scanning electron microscopy (SEM), energy-dispersive X-ray spectroscopy (EDS), and a universal testing machine (UTM) were used to examine the surface morphology, elemental distribution, and mechanical properties of scaffolds. Cell experiments were conducted to investigate the effects and mechanisms of five groups of titanium alloy scaffolds on the osteogenic properties of bone marrow MSCs (BMSCs) and the angiogenic capacity of human umbilical vein endothelial cells (HUVECs). The New Zealand rabbit lateral femoral condyle bone defect models were employed to evaluate the angiogenesis and osteogenesis capabilities of each scaffold group. The surface area, specific surface area per unit volume, and internal flow distribution characteristics of G and DG structure scaffolds were further explored and compared. This study aimed to investigate the role of titanium alloy porous scaffolds with DG structures in angiogenesis and bone repair and determine the optimal porosity for bone growth, providing a foundation for further research on porous bone scaffold structures suitable for human applications.

2 Materials and methods

2.1 Design and preparation of porous Ti6Al4V scaffolds

This study used the computer-aided design software Rhinoceros 6 and Grasshopper Plug-in (McNeal, Seattle, WA, USA) to design Ti6Al4V porous scaffolds. The structural shape of a TPMS-based scaffold was determined by a given mathematical function expression, and the structure was adjusted by changing the corresponding function parameters. This study chose DG units to fabricate TPMS-based porous scaffolds. Four DG scaffolds with different porosities (40%, 55%, 70%, and 85%) were designed, which are sequentially named DG40, DG55, DG70, and DG85. The DG structure was defined by the following equation:

$$\begin{aligned} 2.75\big(&\sin(2x)\cdot\sin(z)\cdot\cos(y)+\\ &\sin(2y)\cdot\sin(x)\cdot\cos(z)+\\ &\sin(2z)\cdot\sin(y)\cdot\cos(x)\big)-1\big(\cos(2x)\cdot\cos(2y)+\\ &\cos(2y)\cdot\cos(2z)+\cos(2z)\cdot\cos(2x)\big)=0 \end{aligned}$$

The control group scaffold had a traditional cubic structure with a designed porosity of 70%, and it was named Cube. The porous Ti6Al4V scaffold was manufactured using electron beam melting (EBM) technology (Q10 plus, Arcam AB GE Additive, USA). The Arcam Ti6A14V ELI powder used in the manufacturing process had a particle size of 45 to 100 μm. After fabricating scaffolds, the powder was first removed from micropores. A sandblaster was used to remove most of the powder from the structure, and an ultrasonic cleaner was used to remove as much of the remaining powder from the scaffold as possible. The effectiveness of powder removal was assessed through high-precision weighing (Fig. S2 in the supplementary information) and micro-computed tomography (CT) scanning. Scaffolds with minimal weight discrepancies and those with micro-CT scans were selected, showing negligible powder residues for subsequent experiments. Before conducting cell and in vivo experiments, scaffold groups underwent sterilization and drying processes.

2.2 Material characterization of porous scaffolds

The surface morphology and chemical composition of the fabricated samples were analyzed by field emission SEM (SU-8100; Hitachi, Japan) and EDS (IXRF3310; USA). The three-dimensional (3D) structure of each group of Ti6Al4V scaffolds was scanned and analyzed using micro-CT.

2.3 Mechanical properties of porous scaffolds

Compression tests were performed to evaluate the mechanical properties of each group of porous Ti6Al4V scaffolds. Porous Ti6Al4V scaffolds are cylindrical, 8 mm in height and 5 mm in diameter. Four samples were tested in each group (n=4). The tests were carried out using an electronic UTM (WDW10 kN; Sinter, China) with a loading speed of 1.0 mm/min. The elastic modulus of the porous titanium alloy scaffolds was determined from the linear deformation region of the stress-strain curve obtained from compression tests. Yield strength was determined from the first peak of the stress-strain curve.

2.4 In vitro experiments

2.4.1 Cell culture

Rabbit BMSCs were isolated from 1-week-old New Zealand White rabbits. Rabbit BMSCs were cultured in Dulbecco's modified Eagle's medium/nutrient mixture F-12 (DMEM/F-12; Cytiva, USA) containing 10% fetal bovine serum (FBS; HyClone, USA) and 1% streptomycin-penicillin (Gibco, USA). BMSCs passed on to the second generation were selected for experimental cell studies. HUVECs (iCell Bioscience Inc, China) were cultured in high-glucose DMEM (HyClone) supplemented with 10% FBS and 1% streptomycin-penicillin. Cells were cultured in an incubator at 37 °C, 5% CO_2 concentration, and 95% humidity.

2.4.2 Biocompatibility evaluation

Each set of scaffolds was placed into a 48-well plate, and BMSCs were inoculated on each set of scaffolds (Cube, DG40, DG55, DG70, and DG85) at a density of 5×10^4 per well for culture. The medium was changed every 24 h.

Live/dead assay: a calcein-acetoxymethyl ester (AM)/propidium iodide (PI) double staining kit (BestBio, China) was used to assess the effect of each group of scaffolds on BMSC viability. After coculture of BMSCs with each group of scaffolds, scaffolds were collected at the predicted times (1, 3, and 5 d). This approach provided a continuous timeline for visually observing cell growth and survival on scaffolds in each group. Scaffolds were transferred to new 48-well plates before each staining. Live and dead cells were stained with calcein-AM and PI according to the manufacturer's protocol. After staining, cells were transferred to a fluorescence microscope (Olympus, Japan) protected from light for observation.

Cell morphology assay: BMSCs were collected on Day 3 after coculture with each group of scaffolds. Scaffolds were transferred to new 48-well plates. Staining was performed with fluorescein isothiocyanate-phalloidin (Yeasen, China) for filamentous actin and 4′,6-diamidino-2-phenylindole (DAPI) for nuclei. After staining, cells were transferred to a fluorescence microscope (Olympus) protected from light for observation.

Cell proliferation assay: the proliferation status of BMSCs on each group of scaffolds was examined using a cell counting kit-8 (CCK-8; Bioss, USA). Scaffolds were collected on Days 1, 3, and 5 after coculture. At each time point, scaffolds were transferred to new 48-well plates. The 10% CCK-8 working solution was added to each well. After incubation at 37 °C for 2 h protected from light, the absorbance (OD) values of each group were determined at 450 nm using an enzyme marker.

2.4.3 Evaluation of vascularization performance

Wound healing assay: each set of scaffolds was placed into a 12-well plate, and HUVECs were inoculated into each well at a density of 2×10^5 per well. When HUVEC confluence reached 100%, a straight line through the middle of cells was drawn in each well using a sterile gun tip. The medium was replaced with a serum-free medium. Initial and healing images of the scratches were taken with an inverted microscope (Olympus) at 0 and 24 h, respectively. The area of the scratch before and after healing was measured using ImageJ version 1.54, and the rate of scratch wound healing was calculated.

Transwell migration assay: transwell cell culture inserts (8 μm pore size; Corning Costar, USA) were used to assess the vertical migration capacity of HUVECs on each set of scaffolds. Each group of scaffolds was placed in a 48-well plate, and HUVECs were inoculated onto each group of scaffolds at a density of 1×10^5 per well. After coculture for 48 h, HUVECs from each group of scaffolds were resuspended and seeded into the upper chamber containing serum-free medium. The lower chamber contained complete DMEM with 5% FBS. After 8 h culture, the filter membrane in the upper chamber was removed, and cells on the upper layer of the membrane were gently wiped off with a cotton swab, after which they were rinsed clean with phosphate-buffered saline (PBS), and the lower layer of cells was stained with crystal violet. After staining, cells were observed and photographed with an inverted microscope. Counting was performed in three random microscope fields using ImageJ version 1.54.

Tube formation assay: tube formation assay was performed using Matrigel matrix (Corning, USA) to detect the effect of each group of scaffolds on promoting angiogenesis.

The groups of scaffolds were placed into 48-well plates, and HUVECs were inoculated onto each group of scaffolds at a density of 1×10^5 per well. After 48 h coculture, HUVECs on each group of scaffolds were resuspended and inoculated onto the surface of the cured matrix gel. After 8 h incubation, HUVECs were observed under the light microscope (Olympus) and photographed. The junctions were calculated using ImageJ version 1.54 and quantified using the Angiogenesis Analyzer plug-in.

Quantitative real-time polymerase chain reaction (qPCR) of angiogenesis-related genes: angiopoietin-1 (*ANG-1*), hypoxia-inducible factor-1α (*HIF-1α*), and vascular endothelial growth factor (*VEGF*) expression was assessed at 5 d of coculture. The RNAsimple Total RNA Kit (Tiangen, Beijing, China) was used to extract total RNA. RNA was converted to complementary DNA (cDNA) using the SureScript™ First-Strand cDNA Synthesis Kit (Genecopoeia, USA). qPCR assays were performed using the BlazeTaq™ SYBR@ Green qPCR Mix 2.0 kit (Genecopoeia) and LightCycler 480 machine (Roche Co., Ltd., Switzerland). The housekeeping gene was glyceraldehyde 3-phosphate dehydrogenase (*GAPDH*). The primers for the above genes are listed in Table S1 (Supplementary Information).

2.4.4 Evaluation of osteogenic properties

Scaffolds were placed in 48-well plates, and BMSCs were inoculated on each set of scaffolds at a density of 1×10^5 per well. BMSCs were cultured in basal medium for 3 d and changed to bone medium (basal medium containing 10 mmol/L β-glycerophosphate disodium, 10 nmol/L dexamethasone, and 50 μg/mL ascorbic acid). The medium was changed every 48 h. The ability of each group of scaffolds to induce BMSC osteogenic differentiation was evaluated after 7 and 14 d of osteogenic induction.

Alkaline phosphatase (ALP) activity and staining assay: ALP staining was performed using the BCIP/NBT ALP Color Development Kit (Beyotime, China). Briefly, scaffolds were removed on Days 7 and 14, respectively, washed with PBS, fixed with 4% paraformaldehyde for 10 min, and stained with the color development solution. Staining was observed and photographed using the stereomicroscope (BX51TF; Olympus). ALP quantification was performed using the ALP Assay Kit (Beyotime). Scaffolds in 48-well plates were removed on Days 7 and 14, respectively, and transferred to new 48-well plates. The ALP activity of BMSCs on each group of scaffolds was assayed according to the manufacturer's instructions.

Alizarin red S (ARS) staining and quantification: the ARS staining solution (Beyotime) was used to evaluate the formation of calcified mineral nodules on each group of scaffolds. Briefly, groups of scaffolds were first taken out, and the samples were washed with PBS, after which they were fixed with 4% paraformaldehyde for 10 min and stained with ARS staining solution for 30 min, after which the samples were washed with PBS and finally observed and photographed with the stereomicroscope (BX51TF; Olympus). After the ARS staining experiment was completed, the samples were transferred to new 48-well plates, and the calcified mineral nodules on the samples were dissolved using 10% cetylpyridinium chloride (Aladdin, China). The OD values of each group of cells were measured at 562 nm using an enzyme labeler.

qPCR of osteogenic-related genes: Runt-related transcription factor 2 (*RUNX2*), osteopontin (*OPN*), osteocalcin (*OCN*), and ALP osteogenic-related gene expression was assessed after 14 d of coculture. The experimental procedure was similar to that for detecting angiogenic genes. The primers for the above genes are listed in Table S2 (Supplementary Information), and the housekeeping gene was *GAPDH*.

2.5 In vitro experiments

2.5.1 Construction of critical bone defects and implantation of scaffolds

Forty healthy male New Zealand Large White rabbits, aged 6–8 weeks and weighing 2.5–3.5 kg, were selected from the Laboratory Animal Center, College of Basic Medical Sciences, Jilin University, China. Rabbits were well treated during the experiment and were randomly numbered and divided into five groups according to the implanted porous titanium alloy scaffolds (Cube, DG40, DG55, DG70, and DG85 groups). Anesthesia was performed by intramuscular injection of xylazine hydrochloride (0.1 g/mL, 0.15–0.20 mL/kg). The rabbit was well immobilized, and local anesthesia was administered by subcutaneous injection of lidocaine into the femoral condyle. Femoral condyles were exposed, and a cylindrical bone defect with a diameter of 5 mm and a depth of 8 mm was made in the middle of the epiphysis with a bone drill. Porous titanium alloy scaffolds from different groups were randomly implanted on both sides of femoral condyles in an in vivo experiment, and rabbits were identified by ear tags. Penicillin was injected continuously for 3 d after surgery.

2.5.2 Vascular perfusion procedures

New Zealand rabbits were perfused with Microfil (MV-120; Flow Tech, USA) on Week 6 after implantation surgery to assess angiogenesis during bone regeneration. First, New Zealand rabbits were anesthetized using intramuscular injection of xylazine hydrochloride (0.1 g/mL, 0.15–0.20 mL/kg). The thorax was opened, and the left ventricle and inferior vena cava were exposed. An infusion needle was cannulated and secured at the left ventricular apex. Heparinized saline and 50 mL mixed Microfil solution were perfused from the

inlet (left ventricular apex) to the outlet (inferior vena cava), and the perfusion was successful when blue contrast fluid flowed out of the outlet. Perfused New Zealand rabbits were stored at 4 °C overnight to ensure polymerization of the contrast medium, and femoral specimens were retrieved and collected the next day.

2.5.3 Micro-CT evaluation

On Weeks 6 and 12 of implant placement, experimental animals were euthanized by carbon dioxide euthanasia, and femoral condyle samples were collected and immediately fixed with 4% paraformaldehyde. The samples were tomographically scanned using a micro-CT scanner (SkyScan 1076 scanner, Belgium). Structural images of new bone tissue and scaffolds were reconstructed and visually evaluated. The cylindrical area in the sample where the scaffold was located was set as the region of interest (ROI). Bone formation was quantitatively analyzed based on micro-CT data, including bone volume/total volume ratio (BV/TV), trabecular separation (Tb.Sp), and trabecular thickness (Tb.Th).

On Week 6 of implant placement, samples containing angiographic contrast agents were obtained by performing a vascular perfusion procedure on experimental animals. The samples were fixed with 4% paraformaldehyde immediately after collection. A micro-CT scanner was used to tomograph a 2 mm area around the sample. Neovascularization images were reconstructed and visually evaluated.

2.5.4 Histological assessment

After micro-CT scanning, paraformaldehyde-fixed samples were dehydrated using a gradient ethanol solution (70% – 100%, mass fraction), after which the samples were embedded in polymethylmethacrylate. The embedded tissue blocks were cut into 150-mm-thick sections using an ultrahard tissue slicer, polished, and sanded to 40 mm. Tissues were stained with hematoxylin-and-eosin (H&E) and histologically analyzed using Masson trichrome staining.

2.5.5 Immunohistochemistry (IHC) assessment

IHC staining was performed for cluster of differentiation 31 (CD31; Bioss, China), VEGF (Bioss, China), HIF-1α (Affinity, China), ALP (ABclonal, China), and RUNX2 (ABclonal). Briefly, specimens were obtained at six weeks. The samples were placed in 4% paraformaldehyde for fixation and decalcified. Scaffolds were slowly removed at the end of decalcification, and the remaining samples were embedded in paraffin. For each sample, serial sections were cut at different levels (with a 1-mm gap between levels). The sections were dewaxed, washed, hydrated, and closed with serum, followed by incubation, staining, restaining, and dehydration with primary and secondary antibodies.

2.6 Computational fluid dynamics analysis

The detailed experiments and methods are attached in Section S1 (Supplementary Information).

2.7 Statistical analysis

Data were statistically analyzed using GraphPad Prism version 8.0 and expressed as the mean±standard deviation. One-way analysis of variance was used to compare the experimental results. $P<0.05$ was considered statistically significant.

3 Results

3.1 Surface morphology and composition of porous Ti6Al4V scaffolds

This study designed two scaffolds based on previous studies and experimental requirements [30, 31]. Cylindrical scaffolds (10 mm diameter and 2 mm height) were used for in vitro cellular experiments. Cylindrical scaffolds (5 mm diameter and 8 mm height) were used for characterization and in vivo experiments. Five groups of porous Ti6Al4V scaffolds were successfully manufactured by EBM technology (Fig. S1 in Supplementary Information). Four groups of porous titanium alloy scaffolds based on the DG structure were designed with porosities of 40%, 55%, 70%, and 85% (Fig. 1a), and porosities were 42.1%±0.3%, 55.4%±0.1%, 71.0%±0.2%, and 76.7%±0.3% after micro-CT measurement (Table S3 in Supplementary Information). The lattice structure-based porous titanium alloy scaffolds were designed with 70% porosity, and the measured porosity was 70.4%±0.2% (Fig. 1a).

Micro-CT images (Fig. S3 in Supplementary Information) and SEM scans (Fig. 1b) of the porous samples showed that the scaffold unit structures in each group are well-aligned and meet design requirements. The pores are interconnected, with no visible cracks or impurities. Metal particles of Ti6Al4V powder melted by the electron beam during EBM manufacturing were present on all scaffold surfaces. EDS results showed that fabricated Ti6Al4V porous scaffolds have typical Ti, Al, and V peaks, and the weight percentages of each element were close to those of standard Ti6Al4V, indicating that no contamination events occurred during the fabrication process.

3.2 Mechanical properties of porous Ti6Al4V scaffolds

To evaluate the structural stability and fracture strength of each group of scaffolds, in vitro compression tests were performed. The designed porosity, actual porosity, and mechanical performance data for each group of scaffolds are shown in Table S3 (Supplementary Information). The stress-strain

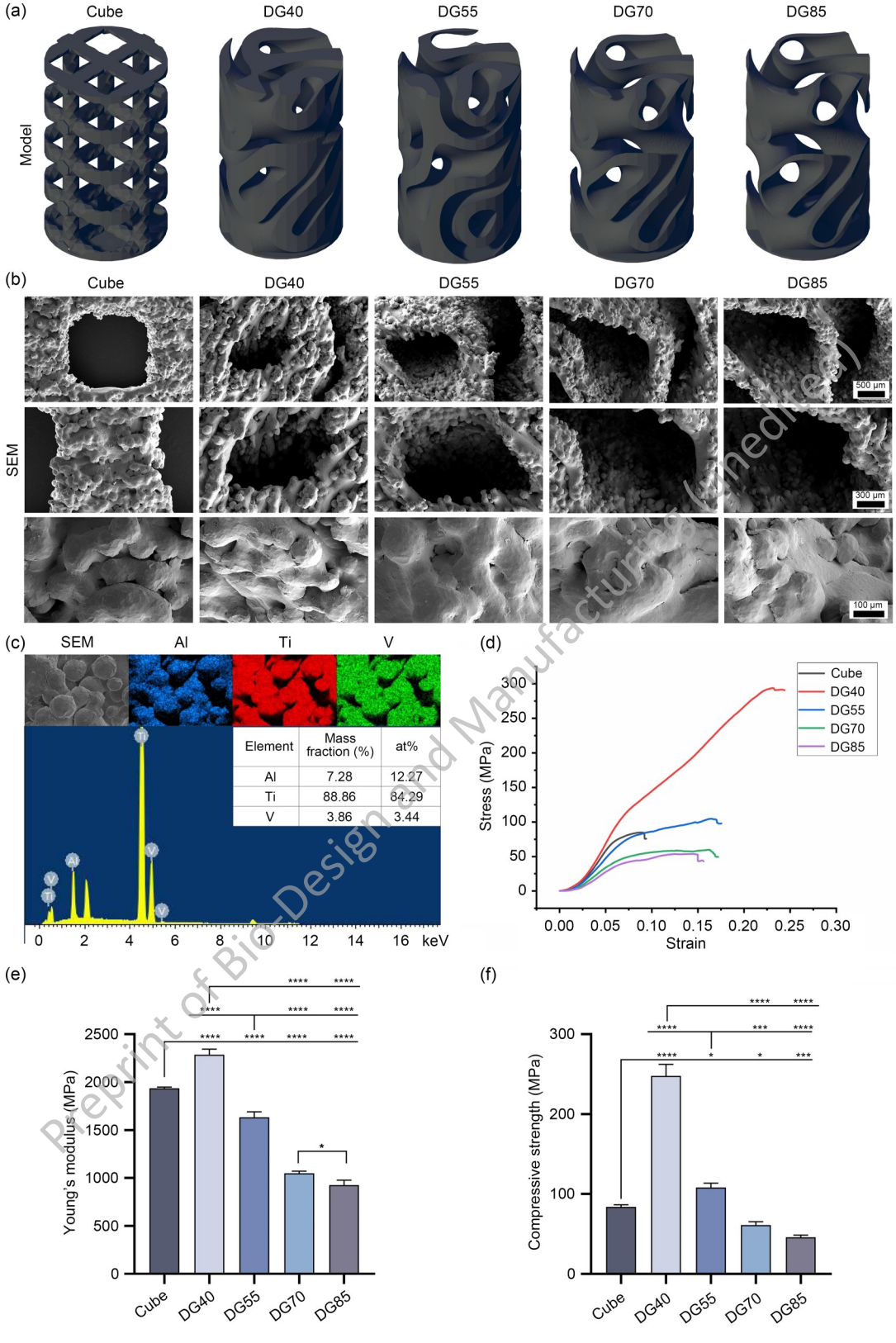

Fig. 1 Characterization of each group of porous titanium alloy scaffolds. (a) Models of conventional lattice-structured scaffolds and four dual gyro-structured scaffolds with different porosities. (b) Observation of microporous features and an indication of the morphology of each group of scaffolds by SEM. (c) Elemental analysis of the prepared titanium alloy scaffolds by EDS. (d) Stress-strain curves of scaffolds. (e) Young's modulus of scaffolds. (f) Compressive strength of scaffolds ($^{*}p<0.05$, $^{**}p<0.01$, $^{***}p<0.001$, $^{****}p<0.0001$; $n=4$). SEM: scanning electron microscopy; EDS: energy-dispersive X-ray spectroscopy; DG: double gyroid.

curves, Young's modulus, and compressive strength of each group of scaffolds are shown in Figs. 1d-1f. Scaffolds showed excellent mechanical properties in terms of strength. Different porosities of porous titanium alloy scaffolds of the same structure led to different compressive strengths and elastic moduli. In the DG groups, the elastic modulus and compressive strength of scaffolds decreased as the porosity increased. When the porosity was 70%, scaffolds in the Cube group exhibited higher elastic modulus and compressive strength than those in the DG70 group.

3.3 Adhesion and proliferation test results of BMSCs on scaffolds

To investigate the cytocompatibility of scaffolds in each group, live/dead cell staining was used to visualize BMSC proliferation on scaffolds (green). In Fig. 2a, the intensity of green fluorescence on scaffolds increased gradually with the prolongation of the cell culture period, indicating a significant increase in the number of BMSCs on scaffolds. CCK-8 assay was used to quantitatively evaluate the cell viability and proliferation activity of BMSCs on different scaffolds (Fig. 2c; Table S4 in Supplementary Information). Over time, groups of scaffolds supported cell proliferation. On Days 1, 3, and 5, the cell viability (OD values) of the DG70 group was 0.5010±0.0079, 0.8777±0.0155, and 1.204±0.0333, whereas those of the Cube group were 0.4327±0.0025, 0.7573±0.0143, and 1.0310±0.0445, respectively. Statistical analysis showed that the OD values of the DG70 group were significantly higher than those of the Cube group, indicating that the DG70 group has significantly better cell proliferation capacity than the Cube group.

Fig. 2b shows F-actin (green) stained with phalloidin and nuclei (blue) labeled with DAPI after 3 d of coculture of each group of scaffolds with BMSCs. Tightly adherent and uniformly distributed BMSCs could be seen on the scaffold surface in each group. BMSCs on scaffolds in each group showed a stretched state and prominent pseudopods. Upon overall observation, the actin filaments of BMSCs on scaffolds of the DG groups were more fully stretched, their cytoskeletal area was larger, and their fiber network was denser than that of the Cube group. The actin filaments of BMSCs on scaffolds of the DG55 group showed the most excellent ductility. BMSCs on scaffolds of the Cube group showed poorer ductility, with smaller individual cytoskeleton areas and closer cell-to-cell distances, preventing cells from fully stretching.

3.4 In vitro angiogenic capacity evaluation

Scratch healing, Transwell, and tube formation assays were performed on HUVECs to assess the angiogenic capacity of scaffolds in each group. Scratch healing experiments showed a healing trend in all groups (Figs. 3a and 3d). Overall, the healing effect was significantly greater in the DG70 group than in the Cube group when the porosity was similar. In the DG groups, as the scaffold porosity gradually increased, the healing trend of cells in all groups was first from low to high, and then from high to low. The DG55 group showed the best healing effect, whereas the healing ability of the DG40 and DG70 groups was a bit poorer. Transwell experiments confirmed similar results (Fig. 3b). In the Cube group, only a few cells migrated in the medium containing low serum concentrations. Quantification of the number of migrating cells showed that significantly more HUVECs migrated in the DG55 group than in the other groups (Fig. 3e). Tube formation assay also showed that the Cube group had a weaker tube formation capacity than the other groups (Fig. 3c), as demonstrated by quantitative analysis based on junctions. Figs. 3g to 3i shows angiogenesis-related genes (*ANG-1*, *HIF-1α*, and *VEGF*) expression after coculture of HUVECs and scaffolds for 5 d at the early stage of bone regeneration. Results showed that the expression levels of *ANG-1*, *HIF-1α*, and *VEGF* were significantly higher in the DG70 group than in the Cube group when the scaffold porosity was similar. Overall, *ANG-1*, *HIF-1α*, and *VEGF* levels were significantly higher in the DG55 group compared to other groups.

3.5 In vitro osteogenic capacity evaluation

Results of osteogenic differentiation are shown in Fig. 4, where ALP is a biomarker of osteogenic differentiation, and its expression indicates BMSC differentiation toward the osteoblast lineage. ALP staining can visualize the effect of each group of scaffolds on the osteogenic differentiation of BMSCs. In Fig. 4a, the blue material after ALP staining could be seen on the surface of all five groups of scaffolds for osteogenesis induction compared to silver-white initial scaffolds. Overall, ALP staining was darkest at 7 d of induction and became lighter after 14 d of induction. At both time points, the DG55 group of scaffolds had the darkest ALP staining compared to scaffolds of the other groups. Further ALP quantification experiments made it clearer that the DG55 group had the highest ALP activity and was significantly different from the other groups (Fig. 4b). Comparing the scaffolds of Cube and DG70 groups with similar porosities, the DG70 group of scaffolds with the TPMS structure had higher ALP activity.

ARS staining visualized the extent to which different groups of porous scaffolds affected the mineralization of the outer matrix of BMSCs (Fig. 4c). On Day 7, BMSCs on the scaffold surface in each group began to form light-red mineralized nodules compared to the initial scaffolds. The DG55 group had the deepest mineralized nodules on the scaffold surface. ARS semiquantitative experiments showed statistically significant differences in the mineralization degree of scaffolds in the DG55 group compared to scaffolds of other groups (Fig. 4d). On Day 14, mineralized nodules on the

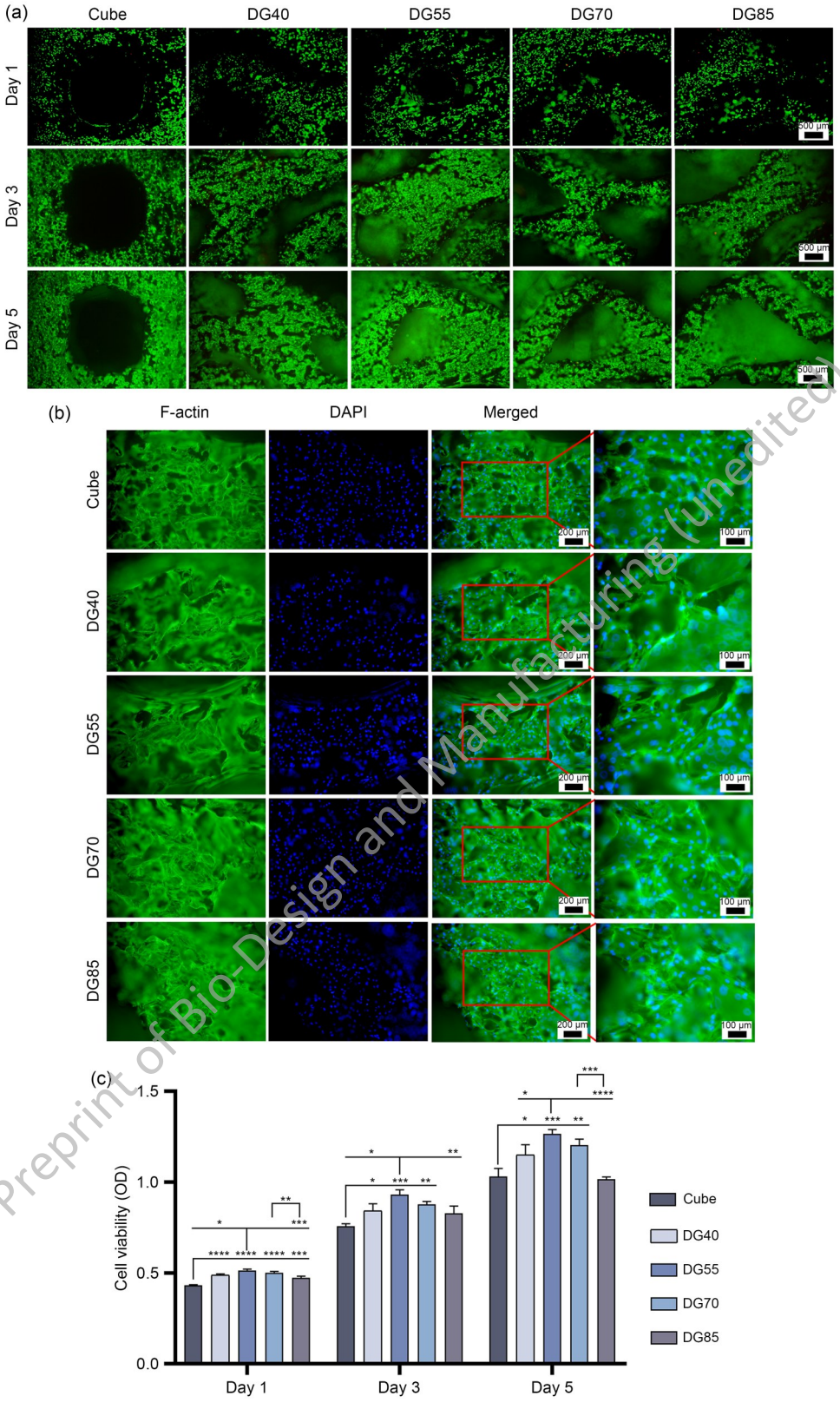

Fig. 2 Biocompatibility, cell morphology, and activity of BMSCs on scaffolds. (a) BMSCs on scaffolds stained with a live/dead staining kit after 1, 3, and 5 d of coculture. (b) Representative cytoskeletal and nuclear staining images of BMSCs on each group of scaffolds after 72 h. (c) BMSC proliferation cultured on each group of scaffolds as assessed by the CCK-8 kit on Days 1, 3, and 5 ($^{*}p<0.05$, $^{**}p<0.01$, $^{***}p<0.001$, $^{****}p<0.0001$; $n=3$). BMSCs: marrow mesenchymal stem cells; CCK-8: cell counting kit-8; DAPI: 4′,6-diamidino-2-phenylindole; DG: double gyroid; OD: absorbance.

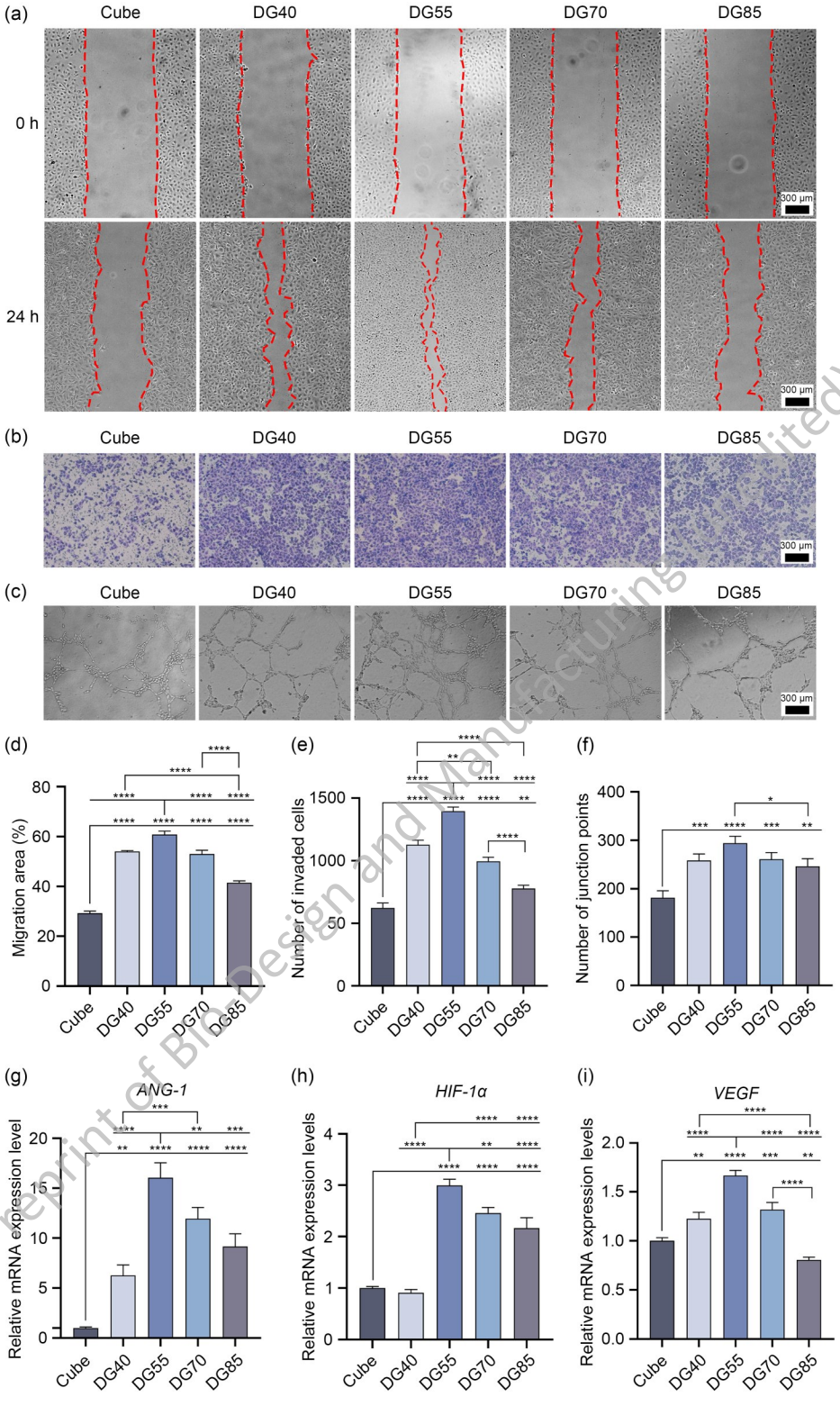

Fig. 3 Angiogenic capacity of HUVECs on scaffolds in each group. (a) Representative images of HUVECs migrating in different groups at specific time points (0 and 24 h). (b) Representative images of HUVECs migrating to the lower surface after 8 h (stained by crystal violet). (c) Representative images of tube formation of HUVECs after 8 h incubation on a matrix gel. (d) Quantitative analysis of the scratch healing assay. (e) Quantitative analysis of migration in the Transwell assay. (f) Quantitative analysis of endothelial cell-forming branching points in the tube formation assay. *ANG-1* (g), *HIF-1α* (h), and *VEGF* (i) gene expression after 5 d of coculture in scaffolds ($^{*}p<0.05$, $^{**}p<0.01$, $^{***}p<0.001$, $^{****}p<0.0001$; $n=3$). HUVECs: human umbilical vein endothelial cells; *ANG-1*: angiopoietin-1; *HIF-1α*: hypoxia-inducible factor-1α; *VEGF*: vascular endothelial growth factor; DG: double gyroid.

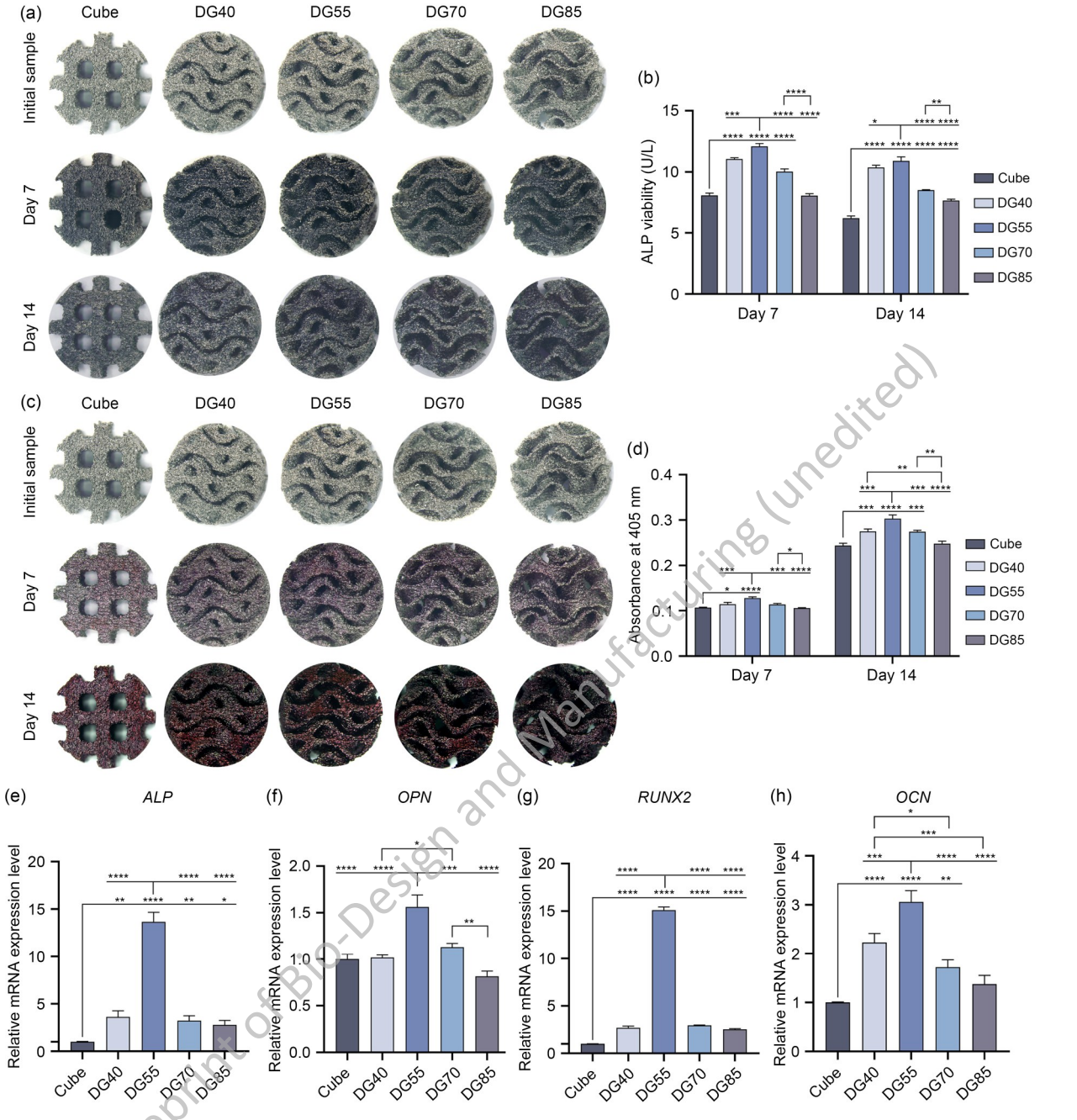

Fig. 4 Osteogenic differentiation ability of BMSCs on each group of scaffolds. (a) ALP staining of each group of scaffolds after coculture with BMSCs for 7 and 14 d. (b) ALP quantification experiments of each group of scaffolds after coculture with BMSCs for 7 and 14 d. (c) ARS staining experiments of each group of scaffolds after coculture with BMSCs for 7 and 14 d. (d) Scaffolds of each group and BMSCs were cocultured for 7 and 14 d for ARS semiquantitative experiments. *ALP* (e), *OPN* (f), *RUNX2* (g), and *OCN* (h) expression levels of scaffolds in different groups cocultured with BMSCs ($^{*}p<0.05$, $^{**}p<0.01$, $^{***}p<0.001$, $^{****}p<0.0001$; $n=3$). BMSCs: marrow mesenchymal stem cells; *ALP*: alkaline phosphatase; ARS: alizarin red S; *OPN*: osteopontin; *RUNX2*: Runt-related transcription factor 2; *OCN*: osteocalcin; DG: double gyroid.

scaffold surface in each group further deepened to dark red, with DG55 group scaffolds remaining the most deeply mineralized. There was a statistical difference in the degree of mineralization between scaffolds of the Cube and DG70 groups, which had similar porosities, and scaffolds of the DG70 group had a better degree of mineralization. Results of the osteogenesis-related qPCR assay showed that on the Day 14 of coculture of BMSCs with scaffolds, the DG55 group showed the highest expression of osteogenic genes, especially *ALP* and *RUNX2*, compared to other groups (Figs. 4e–4h). At similar porosity, *ALP*, *RUNX2*, and *OPN* expression levels were higher in DG70 group scaffolds than those in Cube group, whereas *OCN* expression was not significantly different between the two groups.

3.6 Micro-CT

The repair effect of the five groups of scaffolds was evaluated by constructing the critical-size rabbit lateral femoral condyle bone defects (Fig. S4). Micro-CT measurements were performed on postoperative Weeks 6 and 12 to assess new bone formation. Micro-CT reconstructed images (Fig. 5a) and quantitative measurement data of BV/TV (Fig. 5b), Tb.Th (Fig. 5c), and Tb.Sp (Fig. 5d) demonstrated the bone formation on scaffolds in each group in detail. Over time, new bone tissue readily grew into the deeper layers of the scaffold network. A significant excess of new bone tissue in scaffolds of DG55 and DG70 groups over the other groups was observed within the 6th week. After 12 weeks, further growth of bone tissue was observed in all groups, with more new bone tissue in the DG55 group than in the DG70 group, and the difference was statistically significant. With similar porosity, there was more new bone tissue in the DG70 group than in the Cube group, with a statistically significant difference. The Tb.Th of the new bone tissue showed that it was greater in DG40 and DG55 groups than in the other groups on Week 6; the difference in Tb.Th between the groups gradually decreased on Week 12 (Fig. 5c). The Tb.Sp of the new bone tissue formation showed that the Tb.Sp of Cube and DG40 groups was greater than that of the other groups on Week 6; the difference between the Tb.Sp of the Cube and DG40 groups and that of the other groups increased on Week 12, and the difference was statistically significant (Fig. 5d).

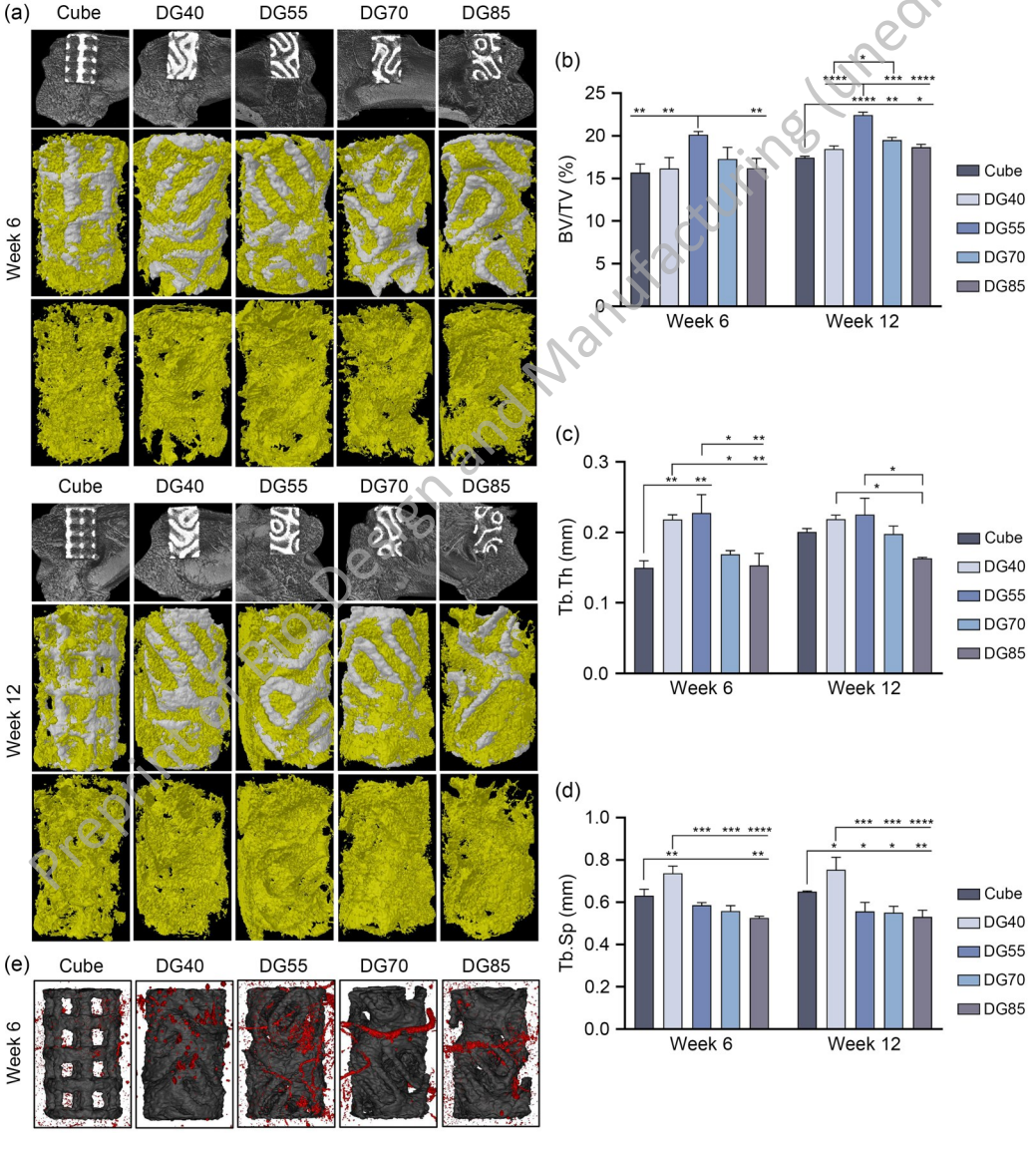

Fig. 5 Micro-CT analysis of new bone formation at 6 and 12 weeks. (a) Reconstructed images of new bone and scaffolds at 6 and 12 weeks. At 6 and 12 weeks, the regenerated bone in the porous scaffolds was analyzed for BV/TV (b), Tb.Th (c), and Tb.Sp (d). (e) Representative reconstructed images of neovascularization on Week 6 ($^{*}p<0.05$, $^{**}p<0.01$, $^{***}p<0.001$, $^{****}p<0.0001$; $n=3$). BV/TV: bone volume/total volume; Tb.Th: trabecular thickness; Tb.Sp: trabecular separation; DG: double gyroid.

This study used microangiography to analyze vessel formation around scaffolds in each group. Because the CT values of the Microfil contrast agent and Ti6Al4V were almost the same, and the angiographic images inside scaffolds were susceptible to artifacts of Ti6Al4V, it was more difficult to differentiate between the vessels and Ti6Al4V. Therefore, based on previous studies, a 2-mm region around the scaffold as the ROI was selected to indirectly reflect vascular formation [32]. On postoperative Week 6, reconstructed images of peri-scaffold angiogenesis in five groups were obtained by contrast perfusion, decalcification, and micro-CT scanning and reconstruction (Fig. 5e). Compared to the Cube group, the DG70 group exhibited tubular vessels growing around scaffolds. Among DG groups, the DG55 group showed more tubular vessels surrounding scaffolds. The above results indirectly reflected that DG group scaffolds were more favorable for early vessel growth and attachment. DG group scaffolds with 55% porosity had the best ability to induce vessel formation.

3.7 Histological analysis

This histologic analysis aimed to examine the presence of osteogenic bone in each group of scaffolds. Longitudinal sections of bone specimens could show the status of scaffolds and new bone formation in bone defects. When H&E-stained sections were observed six weeks after implantation, no obvious inflammatory reaction or necrosis was observed in all groups, indicating that scaffolds had good biocompatibility (Fig. 6a). Newly formed bone tissue was observed at the interface between the scaffold and the defect in all groups. H&E staining at 12 weeks of implantation showed a gradual increase in new bone tissue in all groups, with a further

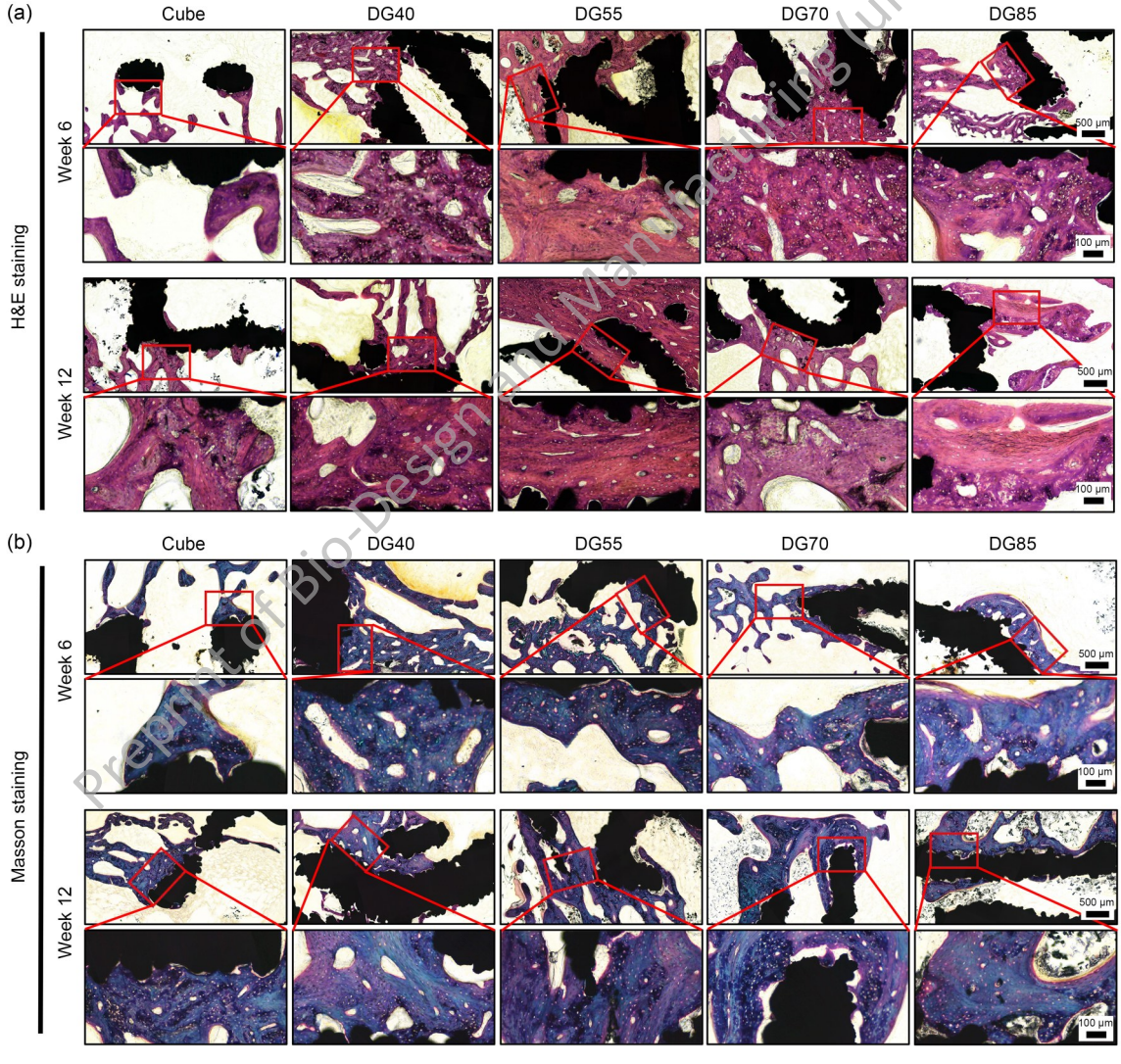

Fig. 6 Histological staining of hard tissue sections of scaffolds implanted in vivo on Weeks 6 and 12. The black area is the scaffold section, and the magnified image is shown in the red box. (a) H&E staining reveals new bone tissue stained in pink. (b) Masson trichrome staining. Bone tissue with low maturity was stained blue; as bone maturity increased, the content of type I collagen fibers rose, and bone tissue with high maturity was stained red. H&E: hematoxylin-and-eosin; DG: double gyroid.

increase in the depth of long entry. The newly formed bone tissue was more pronounced in the DG55 group, and the thickness of the formed bone tissue was relatively larger. Masson trichrome staining results confirmed that the DG70 group had more type I collagen fibers than the Cube group, which had similar porosity (Fig. 6b). Among DG groups, the DG55 group had the most type I collagen fibers.

3.8 IHC analysis

IHC staining tests on samples at Week 6 (peri-scaffold area) were performed to further investigate vascular regeneration and bone regeneration at the scaffold-bone interface (Fig. 7a). Anti-ALP and anti-RUNX2 were used to label osteogenic marker expression in tissues. Compared to the Cube group, osteoblasts on the bone trabeculae surrounding scaffolds in the DG70 group had more positive expression. Anti-CD31 and anti-VEGF were used to label blood vessels in the tissue. A higher vessel density was seen in the DG70 group compared to the Cube group. HIF-1α expression was also examined in the tissues. Positive HIF-1α expression was observed in the vessels of the scaffold periprosthetic tissue in the DG70 group compared to the Cube group.

4 Discussion

Segmental bone defects are a significant challenge for orthopedic surgeons. Although autologous bone grafting is the gold standard for treating such bone defects, the scarcity of bone donors, the cost, and the risk of the procedure hinder clinical applications [33]. With the development of BTE technology, Ti6Al4V implants are widely used in treating segmental bone defects due to their good biological properties, excellent mechanical strength, and mature processing technology [34]. Bionic porous optimization strategies for titanium alloy scaffolds effectively promote osseointegration at the prosthesis and implant interface [35, 36]. TPMS structures are receiving increasing attention for their excellent mechanical properties and desirable biomorphic features [16]. Specifically, because the mean surface curvature of the TPMS structure is zero, prostheses with this structure allow for an even distribution of the stresses to which they are subjected, avoiding implant failure due to stress shielding [37]. The zero-curvature surface of TPMS induces stress fiber reorganization and nucleus deformation of cells, promoting the osteogenic differentiation ability of human MSCs and the vascular differentiation ability of HUVECs [20]. Therefore, porous titanium alloy scaffolds based on TPMS structures are expected to expand the new application prospects of titanium alloy materials. At present, exploring the osteogenic properties of TPMS structures in BTE mainly focuses on comparing different TPMS structures or TPMS with strut-node lattice structures. For example, Shen et al. [38] investigated the relationship between early bone conduction behavior and a series of scaffolds with TPMS pore structures (diamond, s-diamond, gyroid, s-gyroid, and Schoen's I-graph-wrapped package (IWP)). Lu et al. [39] evaluated the bone regeneration capability of scaffolds with

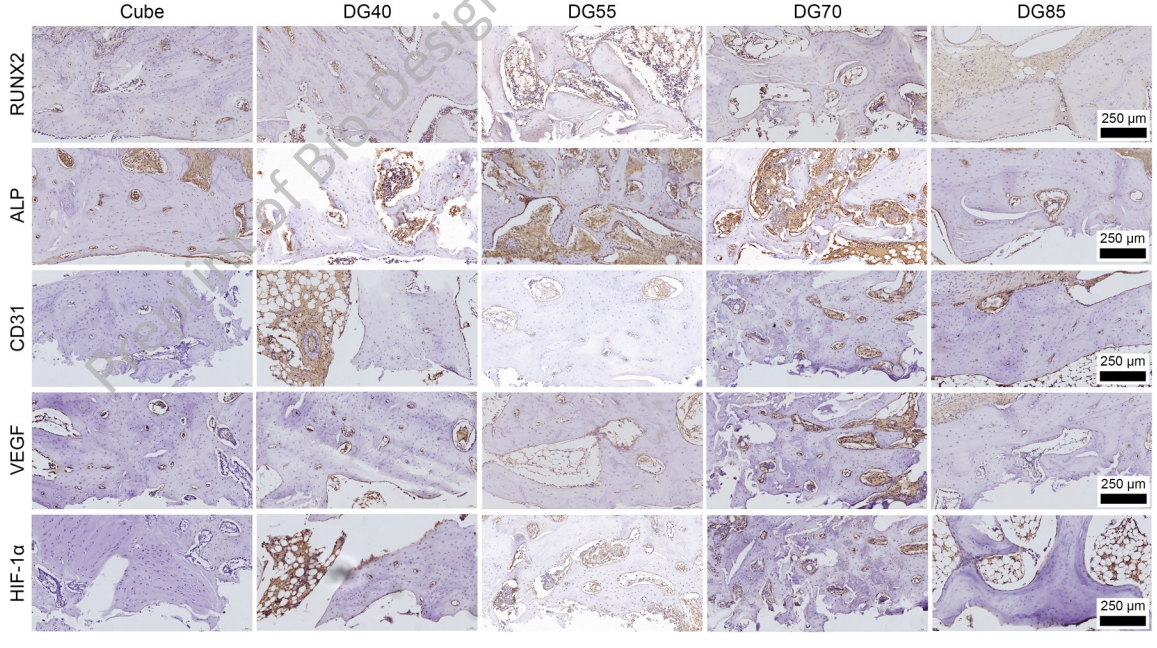

Fig. 7 IHC tissue staining at the scaffold junction and bone defect on Week 6. Anti-ALP and anti-RUNX2 were used to label osteogenesis-related protein expression in tissues. Anti-CD31 and anti-VEGF were used to label angiogenesis-related protein expression in tissues. Anti-HIF-1α was used to label hypoxia-related protein expression in tissues. ALP: alkaline phosphatase; RUNX2: Runt-related transcription factor 2; CD31: cluster of differentiation 31; VEGF: vascular endothelial growth factor; HIF-1α: hypoxia-inducible factor-1α; DG: double gyroid.

three representative pore morphologies (cross-column, diamond, and gyroid). However, fewer studies reported the optimal porosity for specific TPMS structures suitable for vascular and bone regeneration. Inspired by natural bone trabecular structures, this study designed and fabricated a DG titanium alloy scaffold based on TPMS structures and explored the optimal porosity of this scaffold structure suitable for angiogenesis and osteogenesis.

In this study, four DG scaffolds with the TPMS structure and one cubic scaffold with the classical lattice structure were successfully manufactured using EBM technology with designed porosities of 40%, 55%, 70%, 85%, and 70%, respectively.

This study conducted visual inspection, SEM examination, and micro-CT scanning of the prepared scaffolds and endeavored to select scaffolds with fewer cracks for subsequent experiments. SEM images showed the presence of uniformly distributed metal particles on the surface of each group of scaffolds. Surface roughness can promote and hinder cell adhesion and growth depending on the severity of the roughness [40]. Moderate roughness provides a larger surface area and more adhesion points, which can enhance cell adhesion and growth [41]. Porous scaffolds implanted in load-bearing sites should have mechanical properties that match those of the surrounding tissue [27]. Young's modulus of the human cancellous bone varies between 0.1 and 2.0 GPa, and the compressive strength of cancellous bone ranges from 2 to 20 MPa [42]. The Young's modulus of porous scaffolds fabricated by EBM ranged from ~926.2±51.3 to 2286.0±58.3 MPa, and their compressive strength ranged from ~46.0±2.7 to 247.9±14.6 MPa. Except for the scaffolds of DG40 group whose Young's modulus was slightly higher than this range, the Young's modulus of the other four groups of scaffolds was within this range, indicating that the elastic modulus of these five scaffolds and the host bone tissue can be well matched, effectively reducing the stress shielding effect. The high compressive strength of scaffolds can provide better mechanical support for the implantation site [5].

This study assessed the cytocompatibility of each group of scaffolds by live/dead staining and CCK-8 assay. The cell morphology of BMSCs on each group of scaffolds was evaluated by immunofluorescence staining. The cytocompatibility assay showed that the number of viable cells on scaffolds in the DG70 group was significantly higher than in the Cube group with similar porosity. Immunofluorescence showed that the fibrillar actin extension of BMSCs located on DG70 group scaffolds was longer, and the overlap of reticular fibers between cells was more densely packed than that in the Cube group. This is mainly attributed to the unique local pore curvature of DG group scaffolds with the TPMS structure. Previous studies have shown that tissue regeneration positively correlates with the curvature of the surface on which it resides [43, 44]. Therefore, scaffolds with a DG structure are more beneficial for tissue regeneration than planar structure scaffolds. In the DG groups, the number of live cells on scaffolds in each group first gradually increased and then gradually decreased as the scaffold porosity gradually increased. The number of live cells of BMSCs on scaffolds in the DG55 group was the highest. As observed by immunofluorescence, BMSCs on DG55 group scaffolds had a longer extension of fibrillar actin with bundle-like distribution. This could be explained by the size of the pore space between the bilayer lamellae of DG scaffolds. Because fabricated DG scaffolds were made by combining two gyroid sheets, the pore space between the two gyroid sheets could be increased by increasing the DG scaffold porosity. A larger space allows for a better supply of oxygen and nutrients, permitting better BMSC proliferation [45]. As the pore space increases, the distance between cells located on the two sheet-like gyroid faces gradually increases, resulting in a gradual increase in the distance between cell junctions. Therefore, BMSCs on DG55 group have a thicker and longer fiber-like actin. However, as the pore space increases, the junction ability between cells weakens, resulting in a more restricted distribution of fibrillar actin on scaffolds in DG70 and DG85 groups. Stress fibers between neighboring cells generate interaction forces, promoting cell proliferation [46]. As the porosity increases, the distance between adjacent gyroid surfaces becomes too large and unfavorable for junction and interaction between neighboring cells. Therefore, fewer viable cells on DG70 and DG85 group scaffolds would be observed.

Bone is one of the tissues with the richest vascular network in the body, and blood vessel formation plays an integral role in bone regeneration [47]. The vascular network provides transportation of cells, oxygen, nutrients, and waste products for bone regeneration and signaling molecules related to bone repair [48]. The effects of the five scaffolds on HUVECs were analyzed using scratch healing experiments, Transwell migration, and tube formation experiments. Results showed that DG70 group scaffolds significantly enhanced the migration, invasion, and tube formation of HUVECs compared to the Cube group scaffolds with similar porosity. DG55 group scaffolds exhibited the optimal ability to promote HUVEC migration and invasion in DG groups. Significant upregulation of angiogenesis-related gene (*ANG-1*, *HIF-1α*, and *VEGF*) expression was observed in DG70 group scaffolds compared to Cube group scaffolds. Among DG groups, the DG55 group had the most significant expression of angiogenic genes. These findings were confirmed by subsequent in vivo experimental angiogenesis micro-CT results. Previous studies have shown that the YAP/TAZ pathway transduces mechanical signals exerted by the extracellular matrix and cell geometry to regulate HUVEC proliferation, migration, and survival and to control angiogenesis and vascular remodeling [49, 50]. Li et al. [27] demonstrated that the unique pore curvature of the TPMS structure compared to the lattice-

like structure activates the YAP/TAZ pathway and mediates HUVEC migration and differentiation, explaining the results observed in the above experiments. YAP/TAZ can also regulate the VEGF signaling pathway, which is important in inducing angiogenesis in vivo [51]. This was consistent with qPCR results that detected high expression of the *VEGF* gene in DG70 group scaffolds. *HIF-1α* is a hypoxia-dependent transcriptional activator secreted by cells under hypoxic conditions, which can also activate VEGF's transcription [52]. In qPCR, *HIF-1α* gene expression on scaffolds in the DG70 group was significantly higher than in the Cube group. Among DG groups, DG55 group scaffolds exhibited the highest *HIF-1α* gene expression, suggesting that DG group scaffolds with the TPMS structure induce HUVECs to highly express *HIF-1α* than lattice structure scaffolds when the porosity was similar, whereas in the DG structure, scaffolds with 55% porosity induced HUVECs to express the most *HIF-1α* genes. ANG-1 has a strong regulatory capacity for neovascularization and significantly improves vessel maturation and stability [53]. HUVECs on DG70 group scaffolds expressed a higher *ANG-1* gene expression than the Cube group. Among DG groups, the DG55 group had the highest *ANG-1* gene expression. The above results suggested that DG group scaffolds with the TPMS structure can significantly promote the maturation of neovascularization compared to traditional cubic structure scaffolds and that DG group scaffolds with 55% porosity have the best ability to promote blood vessel maturation.

ALP is one of the markers of early osteogenic differentiation and can be used as an indicator for evaluating tissue calcification capacity and osteoblast activity [54]. On Days 7 and 14, the DG group exhibited higher ALP activity than the Cube group at 70% porosity. Among DG groups, DG55 scaffolds demonstrated the highest ALP activity, consistent with detecting *ALP* gene expression in qPCR. Mineralization nodules are characteristic markers of osteoblast secretion to form mineralized matrix in vitro [55]. The functional status of terminal differentiation of osteoblasts can be assessed by detecting mineralized nodules. Results of ARS chromogenic and semiquantitative experiments on Days 7 and 14 showed that the DG70 group had a higher degree of mineralization compared to the Cube group. Among DG groups, the DG55 group showed the highest degree of mineralization. To further determine the effect of each group of scaffolds on the osteogenic differentiation of BMSCs, osteogenic-related gene (*ALP*, *OCN*, *RUNX2*, and *OPN*) expression was examined. *RUNX2* is a key transcription factor for osteoblast differentiation, whereas *OCN* and *OPN* are markers expressed during bone matrix mineralization [56, 57]. On Day 14, the expression levels of all tested genes were higher in the DG70 group than in the Cube group. Among DG groups, the DG55 group showed the highest level of osteogenic gene expression, indicating that the osteogenic performance of DG group scaffolds with the TPMS structure was superior to that of the traditional Cube group scaffolds in the early and middle stages of osteogenic differentiation, and DG group scaffolds with 55% porosity had the best osteoinductive performance.

To further validate the conclusions of in vitro experiments, scaffolds were surgically implanted into the lateral femoral condyle of New Zealand rabbits. The micro-CT 3D reconstruction and quantitative analysis showed that newly formed bone tissues existed around and inside scaffolds in each group. On Week 12, bone tissue formed on scaffolds of the DG70 group exhibited higher formation and lower Tb.Sp compared to scaffolds of the Cube group. Bone tissue formed on DG55 group scaffolds exhibited the highest formation and lower Tb.Sp compared to other groups. As observed by hard tissue section staining, there were more newly formed bone trabeculae on scaffolds in the DG70 group than in the Cube group, and more type I collagen fibers were formed. Among DG groups, the DG55 group had the most bone trabeculae and type I collagen fibers. This means DG group scaffolds can induce more mature bone tissues than traditional lattice structure scaffolds. Among DG group scaffolds with the same TPMS structure, scaffolds with 55% porosity induced the most mature bone tissue.

The reason for the differences in bone distribution between different scaffold structures under conditions of similar porosity can be explained by the following theory. First, the DG scaffold surface with smooth and continuous hyperbolic surfaces has higher curvature than cubic scaffolds with flat surfaces. Previous studies have shown that curvature can drive tissue growth and that tissue growth decreases from curved to flat surfaces [58]. Zhang et al. [59] explored the effect of curvature on osteogenesis through computerized and in vivo experiments. They found that curvature can affect cytokine distribution, which influences cellular activity, and that greater curvature induces more bone deposition on the curvier surface. Second, recent studies have shown that angiogenesis and osteogenesis are coupled during bone repair [60]. A capillary subtype closely associated with osteogenesis, the H-vessel, which exhibits strong positivity for CD31 and endomucin (EMCN), can couple vascularization and bone regeneration in bone remodeling [61]. In this study, CD31 IHC positivity was significantly higher in the DG70 group than in the Cube group. Kusumbe et al. [62] found that HIF-1α enhanced H-type angiogenesis and promoted the secretion of potential angiogenic factors by osteoblasts. In IHC, the DG70 group exhibited stronger positive manifestations of *HIF-1α*, *VEGF*, *ALP*, and *RUNX2* compared to the Cube group, suggesting that it may be the specific curvature of scaffolds in the DG groups that promotes osteogenesis by facilitating H-type vessel formation. When scaffold porosity is <70%, the larger the porosity, the more favorable the bone formation; when scaffold porosity is >70%, greater porosity may not be favorable for osteogenesis [28]. In this study, DG scaf-

folds were unfavorable for osteogenesis when the porosity was either >55% or <55%, whereas DG scaffolds with 55% porosity exhibited the best osteogenic performance.

The traditional gyroid structure as a control group was used to further explore the feasibility of the DG structure as a scaffold framework. The surface area and specific surface area per unit volume of gyroid and DG structure scaffolds were measured, as shown in Fig. S5 (Supplementary Information). At the same porosity, the surface area and specific surface area per unit volume of the DG structure scaffolds were significantly greater than those of gyroid structure scaffolds. O'Brien et al. [63] found a strong correlation between the scaffold specific surface area and cell attachment, with the number of cells attached to the scaffold surface linearly increasing with the increase in the scaffold specific surface area, suggesting that under similar porosity conditions, the DG structure is more conducive to cell adhesion and growth compared to the gyroid structure. Furthermore, flow distribution characteristics within the scaffold will affect cell adhesion, growth, and the transport of nutrients and waste [64]. By comparing the fluid characteristics of DG and gyroid structures at 37 °C (Fig. S6), the DG structure exhibits more uniform and lower flow velocity characteristics than the gyroid structure. This uniform low-flow velocity region facilitates cell adhesion and growth on the inner surface of DG scaffolds [65].

5 Conclusion

In this study, four titanium alloy scaffolds with different porosities (40%, 55%, 70%, and 85%) of the DG structure were designed and prepared, and traditional cubic scaffolds with 70% porosity were used as a control group to systematically investigate the performance of the DG structure in bone repair. Compression tests showed that the mechanical strength of the cubic structure was stronger than that of the DG structure at 70% porosity. However, the elastic modulus and compressive strength of the DG group were still within the range of normal cancellous bone. In vitro cellular experiments showed that the local curvature characteristic of the DG structure facilitated the proliferation and differentiation of HUVECs and BMSCs compared to the conventional cubic structure. DG scaffolds with 55% porosity exhibited the best ability to promote osteogenesis and angiogenesis. In vivo experiments demonstrated that new bone tissue and blood vessels could grow well into the DG structure compared to the classical cubic structure, and the DG structure with 55% porosity was most favorable for bone and blood vessel regeneration. Compared to the classic G structure, the DG structure had a larger specific surface area per unit volume and flow distribution characteristics that were more suitable for tissue cell adhesion and growth. These findings indicated that DG scaffolds based on TPMS structures effectively induce angiogenesis and promote bone regeneration by optimizing the design of the pore structure of titanium scaffolds, providing important design references and experimental bases for applying titanium scaffolds in clinical bone defect repair.

Acknowledgements This work was supported by (1) the National Natural Science Foundation of China (Nos. 82272504 and 82072456); (2) the Department of Science and Technology of Jilin Province, China (Nos. 20210101439JC, 20210101321JC, 20220204119YY, 202201ZYTS131, 202201ZYTS129, 20230204114YY, YDZJ202201 ZYTS505, and YDZJ202301ZYTS076); (3) the Special Program for Science and Technology Personnel of Changchun (No. ZKICKJJ2023015); (4) the Key training plan for outstanding youth of Jilin University (No. 419070623036); (5) the Research Fund of the First Hospital of Jilin University (No. 2021-zl-01); (6) the Graduate Innovation Fund of Jilin University (No. 2024CX125); (7) the Foundation of National Center for Translational Medicine (Shanghai) SHU Branch (No. SUITM-202405), China.

Authorship contribution statement Hao Liu: Conceptualization, Data curation, Methodology, Writing-original draft, Formal analysis, and Writing-Review & Editing. Hao Chen: Conceptualization, Methodology, and Writing-Review & Editing. Bin Sun: Conceptualization. Danyang Fan: Writing-review & editing. Aobo Zhang: Data curation. Hanqiang Liu: Formal analysis and Software support. Hexiang Wei: Data Curation and Investigation. Wenbo Yang: Investigation. Yongyue Li: Validation. Peng Xia: Conceptualization, Methodology, Resources, Writing-review & editing, Supervision, Project administration, and Funding acquisition. Qing Han: Conceptualization, Methodology, Supervision, Project administration, Writing-Review & Editing, and Funding acquisition. Jincheng Wang: Supervision.

Declarations

Conflict of interest The authors declare that they have no known competing financial interests or personal relationships that could have appeared to influence the work reported in this paper.

Ethical approval We strictly follow the Institutional Animal Care and Use Committee of China. Animal experiments were approved by the Animal Ethics Committee of the School of Basic Medical Sciences of Jilin University (No. 2023473).

References

1. Ran QC, Yang WH, Hu Y et al (2018) Osteogenesis of 3D printed porous Ti6Al4V implants with different pore sizes. J Mech Behav Biomed Mater 84:1–11. https://doi.org/10.1016/j.jmbbm.2018.04.010
2. Cui Y, Wang J, Tian Y et al (2023) Functionalized decellularized bone matrix promotes bone regeneration by releasing osteogenic peptides. ACS Biomater Sci Eng 9(8):4953–4968. https://doi.org/10.1021/acsbiomaterials.3c00413
3. Schmidt AH (2021) Autologous bone graft: is it still the gold standard?. Injury 52(Suppl. 2):S18–S22. https://doi.org/10.1016/j.injury.2021.01.043
4. Lee DJ, Diachina S, Lee YT et al (2016) Decellularized bone matrix grafts for calvaria regeneration. J Tissue Eng 7:2041731416680306. https://doi.org/10.1177/2041731416680306
5. Deng FY, Liu LL, Li Z et al (2021) 3D printed Ti6Al4V bone scaffolds with different pore structure effects on bone ingrowth. J Biol Eng 15(1):4. https://doi.org/10.1186/s13036-021-00255-8

6. Chen YH, Frith JE, Dehghan-Manshadi A et al (2017) Mechanical properties and biocompatibility of porous titanium scaffolds for bone tissue engineering. J Mech Behav Biomed Mater 75:169–174. https://doi.org/10.1016/j.jmbbm.2017.07.015
7. Chen H, Liu Y, Lu Y et al (2024) Bamboo-inspired porous scaffolds for advanced orthopedic implants: design, mechanical properties, and fluid characteristics. ACS Biomater Sci Eng 10(2): 1173–1189. https://doi.org/10.1021/acsbiomaterials.3c01690
8. Metz C, Duda GN, Checa S (2020) Towards multi-dynamic mechano-biological optimization of 3D-printed scaffolds to foster bone regeneration. Acta Biomater 101:117–127. https://doi.org/10.1016/j.actbio.2019.10.029
9. Arabnejad S, Johnston RB, Pura JA et al (2016) High-strength porous biomaterials for bone replacement: a strategy to assess the interplay between cell morphology, mechanical properties, bone ingrowth and manufacturing constraints. Acta Biomater 30:345–356. https://doi.org/10.1016/j.actbio.2015.10.048
10. Li YH, Yang C, Zhao HD et al (2014) New developments of Ti-based alloys for biomedical applications. Materials 7(3):1709–1800. https://doi.org/10.3390/ma7031709
11. Kuboki Y, Takita H, Kobayashi D et al (1998) BMP-induced osteogenesis on the surface of hydroxyapatite with geometrically feasible and nonfeasible structures: topology of osteogenesis. J Biomed Mater Res 39(2):190–199. https://doi.org/10.1002/(sici)1097-4636(199802)39:2<190::Aid-jbm4>3.0.Co;2-k
12. Rudrich U, Lasgorceix M, Champion E et al (2019) Pre-osteoblast cell colonization of porous silicon substituted hydroxyapatite bioceramics: influence of microporosity and macropore design. Mater Sci Eng C Mater Biol Appl 97:510–528. https://doi.org/10.1016/j.msec.2018.12.046
13. Wu FH, Yang J, Ke XR et al (2022) Integrating pore architectures to evaluate vascularization efficacy in silicate-based bioceramic scaffolds. Regen Biomater 9:rbab077. https://doi.org/10.1093/rb/rbab077
14. Karageorgiou V, Kaplan D (2005) Porosity of 3D biomaterial scaffolds and osteogenesis. Biomaterials 26(27):5474–5491. https://doi.org/10.1016/j.biomaterials.2005.02.002
15. Luan HQ, Wang LT, Ren WY et al (2019) The effect of pore size and porosity of Ti6Al4V scaffolds on MC3T3-E1 cells and tissue in rabbits. Sci China Technol Sci 62(7):1160–1168. https://doi.org/10.1007/s11431-018-9352-8
16. Yuan L, Ding SL, Wen CE (2019) Additive manufacturing technology for porous metal implant applications and triple minimal surface structures: a review. Bioact Mater 4(1):56–70. https://doi.org/10.1016/j.bioactmat.2018.12.003
17. Bobbert FSL, Lietaert K, Eftekhari AA et al (2017) Additively manufactured metallic porous biomaterials based on minimal surfaces: a unique combination of topological, mechanical, and mass transport properties. Acta Biomater 53:572–584. https://doi.org/10.1016/j.actbio.2017.02.024
18. Feng JW, Fu JZ, Yao XH et al (2022) Triply periodic minimal surface (TPMS) porous structures: from multi-scale design, precise additive manufacturing to multidisciplinary applications. Int J Extreme Manuf 4(2):22001. https://doi.org/10.1088/2631-7990/ac5be6
19. Li L, Shi JP, Zhang KJ et al (2019) Early osteointegration evaluation of porous Ti6Al4V scaffolds designed based on triply periodic minimal surface models. J Orthop Translat 19:94–105. https://doi.org/10.1016/j.jot.2019.03.003
20. Yang YH, Xu TP, Bei HP et al (2022) Gaussian curvature-driven direction of cell fate toward osteogenesis with triply periodic minimal surface scaffolds. Proc Natl Acad Sci USA 119(41): e2206684119. https://doi.org/10.1073/pnas.2206684119
21. Samson S, Tran P, Marzocca P (2023) Design and modelling of porous gyroid heatsinks: influences of cell size, porosity and material variation. Appl Therm Eng 235:1212976. https://doi.org/10.1016/j.applthermaleng.2023.121296
22. Santos J, Pires T, Gouveia BP et al (2020) On the permeability of TPMS scaffolds. J Mech Behav Biomed Mater 110:103932. https://doi.org/10.1016/j.jmbbm.2020.103932
23. Zou SJ, Mu YR, Pan BC et al (2022) Mechanical and biological properties of enhanced porous scaffolds based on triply periodic minimal surfaces. Mater Des 219:110803. https://doi.org/10.1016/j.matdes.2022.110803
24. Novak N, Al-Ketan O, Krstulović-Opara L et al (2021) Quasi-static and dynamic compressive behaviour of sheet TPMS cellular structures. Compos Struct 266:113801. https://doi.org/10.1016/j.compstruct.2021.113801
25. Feng JW, Fu JZ, Lin ZW et al (2018) A review of the design methods of complex topology structures for 3D printing. Vis Comput Ind Biomed Art 1(1):5. https://doi.org/10.1186/s42492-018-0004-3
26. Maevskaia E, Guerrero J, Ghayor C et al (2023) Triply periodic minimal surface-based scaffolds for bone tissue engineering: a mechanical, in vitro and in vivo study. Tissue Eng Part A 29(19-20): 507–517. https://doi.org/10.1089/ten.tea.2023.0033
27. Li YF, Li JF, Jiang S et al (2023) The design of strut/TPMS-based pore geometries in bioceramic scaffolds guiding osteogenesis and angiogenesis in bone regeneration. Mater Today Bio 20:100667. https://doi.org/10.1016/j.mtbio.2023.100667
28. Wang ZH, Wang CY, Li C et al (2017) Analysis of factors influencing bone ingrowth into three-dimensional printed porous metal scaffolds: a review. J Alloy Compd 717:271–285. https://doi.org/10.1016/j.jallcom.2017.05.079
29. Li JP, Habibovic P, van den doel M et al (2007) Bone ingrowth in porous titanium implants produced by 3D fiber deposition. Biomaterials 28(18):2810–2820. https://doi.org/10.1016/j.biomaterials.2007.02.020
30. Yang WB, Han Q, Chen H et al (2024) Additive manufactured trabecular-like Ti-6Al-4V scaffolds for promoting bone regeneration. J Mater Sci Technol 188:116–130. https://doi.org/10.1016/j.jmst.2023.10.061
31. Wang C, Xu DL, Lin L et al (2021) Large-pore-size Ti6Al4V scaffolds with different pore structures for vascularized bone regeneration. Mater Sci Eng C Mater Biol Appl 131:112499. https://doi.org/10.1016/j.msec.2021.112499
32. Gao P, Fan B, Yu XM et al (2020) Biofunctional magnesium coated Ti6Al4V scaffold enhances osteogenesis and angiogenesis in vitro and in vivo for orthopedic application. Bioact Mater 5(3): 680–693. https://doi.org/10.1016/j.bioactmat.2020.04.019
33. Reichert JC, Cipitria A, Epari DR et al (2012) A tissue engineering solution for segmental defect regeneration in load-bearing long bones. Sci Transl Med 4(141):141ra93. https://doi.org/10.1126/scitranslmed.3003720
34. Li GY, Wang L, Pan W et al (2016) In vitro and in vivo study of additive manufactured porous Ti6Al4V scaffolds for repairing bone defects. Sci Rep 6:34072. https://doi.org/10.1038/srep34072
35. Collins MN, Ren G, Young K et al (2021) Scaffold fabrication technologies and structure/function properties in bone tissue engineering. Adv Funct Mater 31(21):22. https://doi.org/10.1002/adfm.202010609
36. Cheng A, Cohen DJ, Kahn A et al (2017) Laser sintered porous

Ti–6Al–4V implants stimulate vertical bone growth. Ann Biomed Eng 45(8):2025–2035. https://doi.org/10.1007/s10439-017-1831-7
37. Sychov MM, Lebedev LA, Dyachenko SV et al (2018) Mechanical properties of energy-absorbing structures with triply periodic minimal surface topology. Acta Astronautica 150:81–84. https://doi.org/10.1016/j.actaastro.2017.12.034
38. Shen MD, Li YF, Lu FL et al (2023) Bioceramic scaffolds with triply periodic minimal surface architectures guide early-stage bone regeneration. Bioact Mater 25:374–386. https://doi.org/10.1016/j.bioactmat.2023.02.012
39. Lu QJ, Diao JJ, Wang YQ et al (2023) 3D printed pore morphology mediates bone marrow stem cell behaviors via RhoA/ROCK2 signaling pathway for accelerating bone regeneration. Bioact Mater 26:413–424. https://doi.org/10.1016/j.bioactmat.2023.02.025
40. Hou Y, Xie WY, Yu LX et al (2020) Surface roughness gradients reveal topography-specific mechanosensitive responses in human mesenchymal stem cells. Small 16(10):e1905422. https://doi.org/10.1002/smll.201905422
41. Raucci MG, Guarino V, Ambrosio L (2012) Biomimetic strategies for bone repair and regeneration. J Funct Biomater 3(3):688–705. https://doi.org/10.3390/jfb3030688
42. Bharadwaz A, Jayasuriya AC (2020) Recent trends in the application of widely used natural and synthetic polymer nanocomposites in bone tissue regeneration. Mater Sci Eng C Mater Biol Appl 110:110698. https://doi.org/10.1016/j.msec.2020.110698
43. Zadpoor AA (2015) Bone tissue regeneration: the role of scaffold geometry. Biomater Sci 3(2):231–245. https://doi.org/10.1039/c4bm00291a
44. Bidan CM, Kommareddy P, Rumpler M et al (2012) How linear tension converts to curvature: geometric control of bone tissue growth. PLoS One 7(5):e36336. https://doi.org/10.1371/journal.pone.0036336
45. Takahashi Y, Tabata Y (2012) Effect of the fiber diameter and porosity of non-woven PET fabrics on the osteogenic differentiation of mesenchymal stem cells. J Biomater Sci Polym Ed 15(1):41–57. https://doi.org/10.1163/156856204322752228
46. Rumpler M, Woesz A, Dunlop JWC et al (2008) The effect of geometry on three-dimensional tissue growth. J R Soc Interface 5(27):1173–1180. https://doi.org/10.1098/rsif.2008.0064
47. Liu H, Chen H, Han Q et al (2023) Recent advancement in vascularized tissue-engineered bone based on materials design and modification. Mater Today Bio 23:10058. https://doi.org/10.1016/j.mtbio.2023.100858
48. Hendriks M, Ramasamy SK (2020) Blood vessels and vascular niches in bone development and physiological remodeling. Front Cell Dev Biol 8:602278. https://doi.org/10.3389/fcell.2020.602278
49. Boopathy GTK, Hong WJ (2019) Role of hippo pathway-YAP/TAZ signaling in angiogenesis. Front Cell Dev Biol 7:49. https://doi.org/10.3389/fcell.2019.00049
50. Brusatin G, Panciera T, Gandin A et al (2018) Biomaterials and engineered microenvironments to control YAP/TAZ-dependent cell behaviour. Nat Mater 17(12):1063–1075. https://doi.org/10.1038/s41563-018-0180-8
51. Azad T, Janse van Rensburg HJ, Lightbody ED et al (2018) A LATS biosensor screen identifies VEGFR as a regulator of the Hippo pathway in angiogenesis. Nat Commun 9:1061. https://doi.org/10.1038/s41467-018-03278-w
52. Gonzalez FJ, Xie C, Jiang CT (2018) The role of hypoxia-inducible factors in metabolic diseases. Nat Rev Endocrinol 15(1):21–32. https://doi.org/10.1038/s41574-018-0096-z
53. Wallace RG, Rochfort KD, Barabas P et al (2021) COMP-Ang1: therapeutic potential of an engineered angiopoietin-1 variant. Vascul Pharmacol 141:106919. https://doi.org/10.1016/j.vph.2021.106919
54. Orimo H, Shimada T (2008) The role of tissue-nonspecific alkaline phosphatase in the phosphate-induced activation of alkaline phosphatase and mineralization in SaOS-2 human osteoblast-like cells. Mol Cell Biochem 315(1-2):51–60. https://doi.org/10.1007/s11010-008-9788-3
55. Sun H, Xu J, Wang YYF et al (2023) Bone microenvironment regulative hydrogels with ROS scavenging and prolonged oxygen-generating for enhancing bone repair. Bioact Mater 24:477–496. https://doi.org/10.1016/j.bioactmat.2022.12.021
56. Xu W, Xu L, Chen M et al (2012) The effects of low dose X-irradiation on osteoblastic MC3T3-E1 cells in vitro. BMC Musculoskelet Disord 13:94. https://doi.org/10.1186/1471-2474-13-94
57. Liu JT, Wang RQ, Gong X et al (2023) Ti6Al4V biomimetic scaffolds for bone tissue engineering: fabrication, biomechanics and osseointegration. Mater Des 234:112330. https://doi.org/10.1016/j.matdes.2023.112330
58. Vetsch JR, Muller R, Hofmann S (2016) The influence of curvature on three-dimensional mineralized matrix formation under static and perfused conditions: an in vitro bioreactor model. J R Soc Interface 13(123):20160425. https://doi.org/10.1098/rsif.2016.0425
59. Zhang Y, Wang P, Jin JY et al (2022) In silico and in vivo studies of the effect of surface curvature on the osteoconduction of porous scaffolds. Biotechnol Bioeng 119(2):591–604. https://doi.org/10.1002/bit.27976
60. Filipowska J, Tomaszewski KA, Niedzwiedzki L et al (2017) The role of vasculature in bone development, regeneration and proper systemic functioning. Angiogenesis 20(3):291–302. https://doi.org/10.1007/s10456-017-9541-1
61. Peng Y, Wu S, Li YS et al (2020) Type H blood vessels in bone modeling and remodeling. Theranostics 10(1):426–436. https://doi.org/10.7150/thno.34126
62. Kusumbe AP, Ramasamy SK, Adams RH (2014) Coupling of angiogenesis and osteogenesis by a specific vessel subtype in bone. Nature 507(7492):323–328. https://doi.org/10.1038/nature13145
63. O'Brien FJ, Harley BA, Yannas IV et al (2005) The effect of pore size on cell adhesion in collagen-GAG scaffolds. Biomaterials 26(4):433–441. https://doi.org/10.1016/j.biomaterials.2004.02.052
64. Kanwar S, Vijayavenkataraman S (2021) Design of 3D printed scaffolds for bone tissue engineering: a review. Bioprinting 24:e00167. https://doi.org/10.1016/j.bprint.2021.e00167
65. Wang FS, Cai XJ, Shen Y et al (2023) Cell-scaffold interactions in tissue engineering for oral and craniofacial reconstruction. Bioac Mater 23:16–44. https://doi.org/10.1016/j.bioactmat.2022.10.029